

Anisotropy of 4*f* states in 3*d* – 4*f* single-molecule magnets

A. Rauguth,¹ A. Alhassanat,² H. Elnaggar,^{3,4} A. A. Athanasopoulou,¹ C. Luo,^{5,6} H. Ryll,⁵ F. Radu,⁵ T. Mashoff,² Frank M. F. de Groot,³ E. Rentschler,¹ and H. J. Elmers^{1,2,*}

¹*Department Chemie, Johannes Gutenberg-Universität Mainz, D-55128 Mainz, Germany*

²*Institut für Physik, Johannes Gutenberg-Universität, D-55128 Mainz, Germany*

³*Inorganic Chemistry and Catalysis, Debye Institute for Nanomaterials Science, Utrecht University, Universiteitslaan 99, 3584 CG Utrecht, The Netherlands*

⁴*Sorbonne Université, CNRS UMR 7590, Institut de Minéralogie, de Physique et de Cosmochimie, 4 Place Jussieu, 75005 Paris, France*

⁵*Helmholtz-Zentrum Berlin für Materialien und Energie, D-14109 Berlin, Germany*

⁶*Physik-Department, Technische Universität München, D-85748 Garching, Germany*

 (Received 12 October 2021; revised 25 March 2022; accepted 31 March 2022; published 13 April 2022)

We have measured angular-dependent fluorescence-yield x-ray magnetic circular dichroism spectra on single crystals of the heterometallic 3*d* – 4*f* 12-metallacrown-4 TbMn₄ and DyMn₄ complexes. Simulated spectra using crystal-field multiplet calculations reproduce the experimentally observed spectra. The orientation of the molecules causes linear dichroism spectra of the 4*f* absorption spectra. This natural linear dichroism shows the anisotropic charge distribution of the rare-earth 4*f* state in the tetragonal crystal field despite the small 4*f* crystal-field splitting. The magnetic moment of the molecule is dominated by the rare-earth moment revealing a considerably large contribution of orbital moment. From a sum-rule analysis of experimental and simulated x-ray magnetic circular dichroism, we determined corrected spin and orbital Dy moments at low temperature (14 K) within a magnetic field of 7 T. We find a significant angular dependence of the Dy magnetic moments, indicating the presence of fourth-order magnetic anisotropy.

DOI: [10.1103/PhysRevB.105.134415](https://doi.org/10.1103/PhysRevB.105.134415)

I. INTRODUCTION

Heterometallic 3*d* – 4*f* molecular complexes attract scientific interest because of their possible applications in luminescence [1,2], catalysis [3], and molecular magnetism [4]. In the case of molecular magnetism, single molecular magnet (SMM) behavior is of particular interest. SMM behavior may result from the combination of paramagnetic 3*d* metal ions, offering a tailoring of magnetic properties by ligands with highly anisotropic lanthanides such as Dy(III) or Tb(III) with large orbital angular momenta [5], leading to large magnetic anisotropy barriers for the magnetization reversal.

SMM behavior is characterized by a time-dependent remnant magnetization below the blocking temperature T_B [6]. An important goal is the understanding of mechanisms to increase the energy barrier and T_B . The energy barrier for spin reversal E_{eff} in 3*d*-SMMs is equal to $S^2|D|$ for integer spin systems, where the zero-field splitting parameter D is a measure for the magnetic anisotropy that potentially changes upon chemical reactions [7]. In this case, the ground-state bistability arises from the total spin S with its $[2S + 1]m_s$ microstates. In contrast, for rare-earth SMMs the strong spin-orbit coupling of 4*f* states results in the spin-orbit-coupled ground state $^{2S+1}L_J$. The ground state then splits into $[2J + 1]m_J$ microstates that are responsible for the SMM behavior [5]. One measures the slow magnetic relaxation of SMMs by dynamic suscep-

tibility measurements revealing an imaginary component that represents the potential dynamic hysteresis properties [8]. Furthermore, SMMs may allow more advanced applications such as spintronics and quantum computing [9–13].

In particular for the case of rare-earth SMMs, the microstate splitting and hence the macroscopic magnetic anisotropy depend on the anisotropic charge distribution of the 4*f* states [14,15]. Therefore, any microscopic understanding of how the magnetic anisotropy evolves out of the 4*f* ground state under the influence of the crystal field requires knowledge of the spatial charge distribution of the involved 4*f* state. For direct experimental access to the charge distribution anisotropy, single molecular crystals are required and only a few experiments have been performed in this direction [16].

Metallacrowns (MCs) represent a class of molecular structures that are stable under ambient conditions [17–19]. Their cyclic scaffold readily accommodates 3*d* metal ions while maintaining the planar structural motif. However, when 4*f* metal ions are embedded, the smaller ring structures are significantly distorted, and out-of-plane coordination of the guest ion occurs [20,21]. Many previous studies focused on homometallic or heterometallic molecules based on 3*d* transition metals [15,22–25]. MCs composed of transition-metal ions and rare-earth ions are exciting to study because the large orbital moment of the rare-earth element provides a source of large magnetic anisotropy [26–28]. In this article, we focus our experiments on the rare family of isostructural $(^t\text{Bu}_4\text{N})[\text{Ln}^{\text{III}}(\text{O}_2\text{C}^t\text{Bu})_4][12 - \text{MC} -_{\text{Mn}(\text{III})\text{N}(\text{shi})} - 4] \cdot 5\text{CH}_2\text{Cl}_2$ [$\text{Ln} = \text{Tb}(\text{TbMn}_4)$ and $\text{Dy}(\text{DyMn}_4)$],

*elmers@uni-mainz.de

representing an unprecedented example of $\text{Ln(III)}[12\text{-MC}_{\text{Mn(III)N}(\text{shi})\text{-4}}$] without additional coordinating of any alkali or alkaline earth metal ions [29].

We investigate single molecular crystals of LnMn_4 using x-ray absorption spectroscopy (XAS) and x-ray magnetic circular dichroism (XMCD). The molecular single crystals are insulating and therefore do not allow conventional total electron yield measurements. Instead, we measure the absorption spectra via the fluorescence yield [30]. To account for differences of x-ray absorption spectra and fluorescence yield spectra, we calculated spectra using crystal-field multiplet calculations [31,32]. Angular-dependent measurements at the $M_{4,5}$ absorption edge allows the determination of the crystal-field ground-state symmetry [16]. XMCD results in angular-dependent spin and orbital magnetic moments, revealing the order of magnetic anisotropy.

II. EXPERIMENT

LnMn_4 molecules with $\text{Ln}=\text{Tb(III)}$ and Dy(III) have been synthesized as described in Ref. [33]. Magnetization properties result from magnetometry measurements [33] with a superconducting quantum interference device (SQUID) magnetometer on microcrystalline material. The microcrystalline material stems from the same batch as the single crystals used for the x-ray absorption experiments. The magnetization of TbMn_4 shows a rapid increase with increasing field below 1 T followed by a slow, nearly linear increase without reaching saturation [33]. The magnetic behavior indicates the presence of magnetic anisotropy and/or population of the Ln(III) low-lying excited states. The contribution from Mn moments is negligibly small due to an antiferromagnetic coupling as concluded from magnetometric results of the reference compound YMn_4 [33].

XMCD measurements were carried out at the VEKMAG end station of the PM2 beamline at BESSY II [34]. For the XMCD measurements, the LnMn_4 molecular single crystals (see Fig. 1) were glued with carbon paste on a copper sample holder with the c -axis pointing along the surface normal. The x-ray beam was focused to an ellipse shaped spot of $50 \mu\text{m} \times 100 \mu\text{m}$ and adjusted on the center of the flat single crystal of approximate size $1 \text{ mm} \times 0.5 \text{ mm} \times 200 \mu\text{m}$.

The magnetic field axis and the incident circularly polarized x-ray beam are always aligned parallel to each other. The fluorescence intensity has been measured by a diode detector positioned at a fixed angle of -20° with respect to the single-crystal surface normal. The diode surface is covered by aluminum foil to prevent photoemitted electrons from contributing to the signal. For angular-dependent measurements, the angle θ is varied from 0° to 80° . Most experiments have been performed with the a -axis within the scattering plane. As expected from symmetry considerations, we find that the spectra do not change when the azimuthal angle is changed so that the b -axis is in the scattering plane.

Spectra acquired with a positive and negative field direction have been normalized at the preedge. The normalization accounts for a systematic field-dependent detection efficiency of the radiation detector used for measuring the incident photon intensity. A linear function fitted to the pre- and postedge has been subtracted from the spectra in order to account for

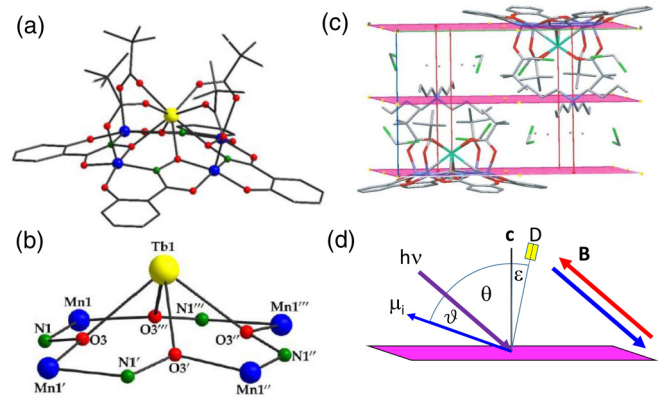


FIG. 1. Molecular structure of the (a) schematic representation of molecular structure and (b) labeled schematic representation of the core $\text{Mn}_4\text{Ln}^{\text{III}}(\mu - \text{NO})_4^{11+}$ of the LnMn_4 complex. Color scheme: Ln, yellow; Mn^{III} , blue, green; N, red. H atoms are omitted for clarity. (c) Unit cell of the (LnMn_4) molecular single crystal. (d) Geometry of the x-ray absorption experiment. The fluorescence detector D is simultaneously rotated with the crystal, $\epsilon = -20^\circ$.

the background intensity caused by x-ray absorption in states with smaller binding energy.

X-ray fluorescence spectra $I_{\text{m.fl}}$ at the Mn $L_{2,3}$ and Ln $M_{4,5}$ edges result from the fluorescence signal as measured by the diode detector current at 14 K. A magnetic field of 7 T was applied parallel and antiparallel to the incident photon beam. The polarization degree is $P = 0.77$ at the Fe L -edge. A calibration measurement at the Gd M -edges confirms that the degree of polarization does not change within the experimental error of 3% within the photon energy range used for the present experiments. The polarization value has been considered for the evaluation of the sum rules [35,36]. We measured each spectrum twice in order to confirm that the x-ray beam does not vary the spectral properties during the spectral run. Even after several hours of absorption measurements, we did not detect any changes of the spectra. Nevertheless, the evaluation of the spectra indicated a reduction of the Mn ions [37–39] (see the Results section).

The fluorescence decay shows a strong dependence on the final state, in contrast to the Auger decay [31,32]. Thus, the fluorescence yield does not measure the pure x-ray absorption spectrum. Therefore, we performed multiplet calculations (see Sec. III) considering a coherent description of the x-ray absorption and x-ray emission processes.

Element-specific magnetic moments of rare-earth ions were determined by the sum-rule analysis [35,36,40–44]. We have set the number of f holes to the ionic values. The jj mixing has been considered via comparison with the simulated spectra.

III. MULTIPLY CALCULATIONS

The magnetic x-ray circular dichroism at the $M_{4,5}$ absorption spectra of rare-earth ions can be simulated by atomic calculations [45,46]. Fluorescence yield spectra differ from pure absorption spectra [31,32]. We performed crystal-field multiplet calculation for the Dy(III) ion in DyMn_4 using the

quantum many-body program QUANTY [47]. The Hamiltonian used for the calculations is

$$H = H_{e-e} + H_{SO} + B_Z. \quad (1)$$

The Hamiltonian terms are the Coulomb interaction, spin-orbit interaction, and Zeeman interaction, respectively. The radial integrals are obtained from atomic Hartree-Fock calculation scaled to 80% to take into account interatomic screening and mixing effects. Atomic values were used for the spin-orbit interaction. The Zeeman interaction was taken into account for a magnetic field of $B = 7$ T. The temperature effect was taken into consideration by using a Boltzmann weighted distribution over the initial state.

IV. EXPERIMENTAL RESULTS

The measured fluorescence signal $I_{m,\text{fl}}$ is modulated by self-absorption of the fluorescence x-ray photons. Qualitatively, the self-absorption leads to a partial suppression of the absorption maxima. The absorption of x-rays as a function of the penetrated depth can be described by an exponential decay function. Approximating the fluorescence x-ray radiation with a monochromatic source, the fluorescence signal sampling depth λ_{fl} is independent from the energy of the incident radiation. In this case, the measured fluorescence intensity $I_{m,\text{fl}}$ is obtained by integrating over the depth z from $z = 0$ to $z = \infty$ as described in Ref. [48]:

$$I_{m,\text{fl}} = C \frac{1}{1 + \lambda_{\text{fl}}/\lambda_X \cos \theta} Y_{\text{fl}}, \quad (2)$$

where $\lambda_X \cos \theta$ is the angular-dependent x-ray penetration depth. Since λ_X strongly varies with the incident x-ray energy, $I_{m,\text{fl}}$ is not proportional to the fluorescence intensity corrected for self-absorption, Y_{fl} , but modulated by an energy-dependent correction factor.

The proportionality constant is given by $C = I_0 G \lambda_{\text{fl}} / \cos \theta$, where the fluorescence gain function G , which depends only weakly on the photon energy, describes the average number of detected fluorescence photons per absorbed x-ray photon [48]. C increases with λ_{fl} and at grazing x-ray incidence according to the $\cos \theta$ term because the photons are absorbed closer to the surface and produce more detectable fluorescence photons.

The incident x-ray penetration depth is related to Y_{fl} by $Y_{\text{fl}} = 1/\lambda_X$. Solving Eq. (2) for Y_{fl} , one obtains

$$Y_{\text{fl}} = \frac{a}{1 - b I_{N,\text{fl}}} I_{N,\text{fl}}. \quad (3)$$

The absorption coefficient thus results from the normalized measured spectrum, $I_{N,\text{fl}} = I_{m,\text{fl}}/I_0$, by applying an energy-dependent correction factor that can also be derived from the measured spectrum. The parameter $b = 1/G$ results from a fit of the branching ratio to the corresponding value of a reference spectrum measured by the total electron yield method on a polycrystalline thin film sample prepared by drop-casting. The parameter b has been determined at the Mn $L_{2,3}$ edges and at the Tb/Dy $M_{4,5}$ edges, separately. The parameter $a = \cos \theta / G \lambda_{\text{fl}}$ represents an energy-independent factor that is used to normalize Y_{fl} to its maximum value at the M_5 (L_3) maximum.

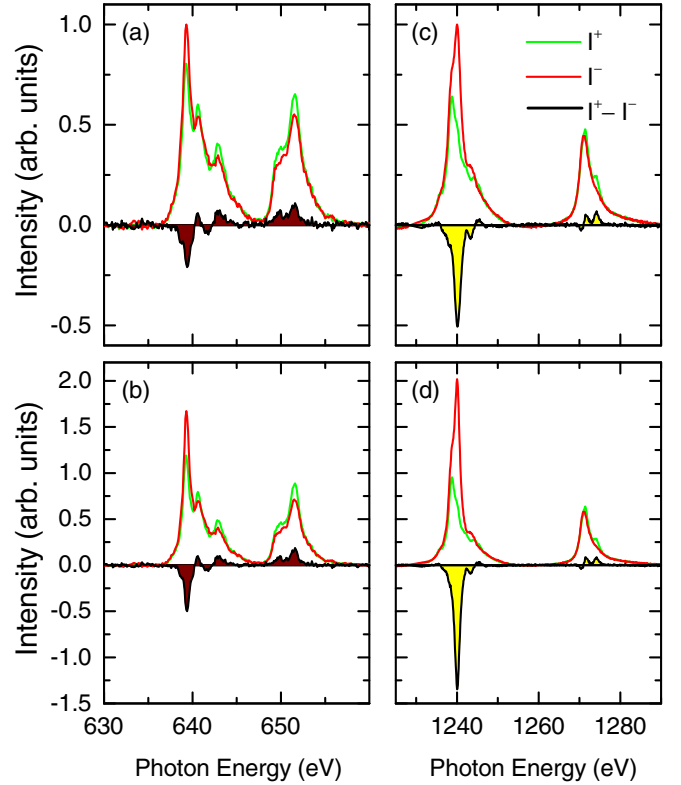


FIG. 2. (a) X-ray fluorescence intensity $I_{m,\text{fl}}$ as a function of photon energy at the Mn $L_{2,3}$ absorption edge in TbMn₄. Spectra are measured for circularly polarized x-ray light parallel and antiparallel (I^+ , I^-) to the magnetic field. The XMCD signal calculated from the difference is depicted as a black line. (b) Corresponding Mn fluorescence signal Y_{fl} generated from the fluorescence spectra in panel (a) by Eq. (3). (c),(d) Similar data obtained at the Tb $M_{4,5}$ absorption edge in TbMn₄. All spectra are measured at normal incidence.

A. TbMn₄

Figure 2 compares the as-measured fluorescence signal $I_{m,\text{fl}}$ with the corrected fluorescence signal Y_{fl} derived from Eq. (3) for TbMn₄. The Mn fluorescence yield [Figs. 2(a) and 2(b)] resembles the typical absorption spectrum for Mn(II) rather than Mn(III). This is in contrast to the expected oxidation state from the single-crystal structure analysis. The total electron yield spectrum measured for the drop-casted sample (not shown here) confirmed the Mn(III) state for the as-prepared sample. In this case, the rapid neutralization of photoemitted charge from the substrate stabilizes the Mn(III) state [39]. Therefore, our results suggest that the x-ray radiation causes a photoreduction of the Mn(III) ions in the single crystal. The reduction happens on a timescale much faster than the measurement of one spectrum. Moreover, the reduction changes the magnetization state of the Mn ions. For the Mn(III) state, the antiferromagnetic exchange interaction results in a vanishing XMCD signal. Instead, the Mn XMCD fluorescence signal of the single crystal is significant, indicating a Mn(II) ion derived magnetic moment.

The Tb fluorescence signal Y_{fl} [Fig. 2(d)] shows a smaller self-absorption correction than in the case of Mn. This can be explained by the four times smaller number of Mn ions. The Tb fluorescence yield shows a large XMCD signal at the M_5

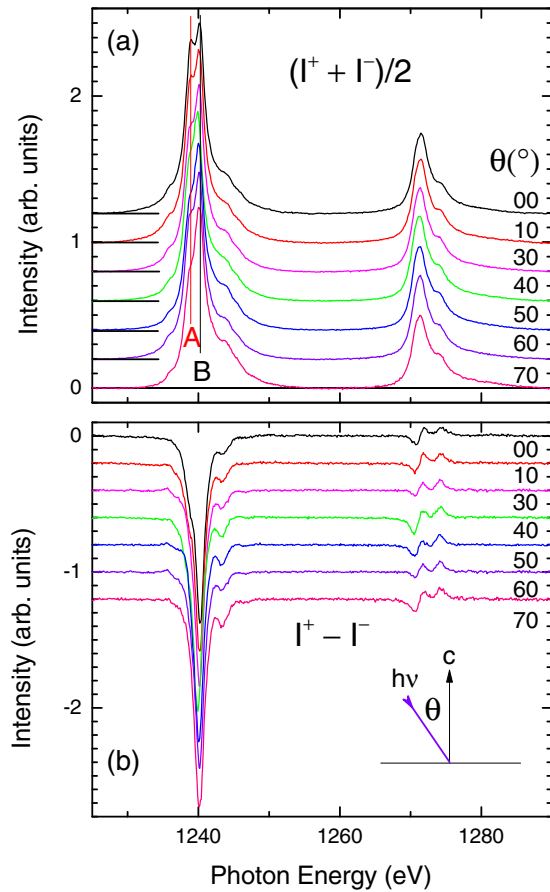


FIG. 3. (a) X-ray fluorescence yield Y_{fi} spectra at the Tb $M_{4,5}$ absorption edge in TbMn_4 ($I^+ + I^-$) measured at the indicated incident angles θ . (b) Corresponding XMCD spectra ($I^+ - I^-$).

edge and a much smaller signal of opposite sign at the M_4 edge.

The sum-rule analysis of the Tb fluorescence signal Y_{fi} reveals an effective spin magnetic moment of $3.3\mu_B$ and an orbital magnetic moment of $3.0\mu_B$. The effective spin moment comprises a contribution from T_z [44].

Next, we measured angular-dependent Tb spectra as shown in Fig. 3. The spectral shape of Y_{fi} at the M_4 edge varies only little with the angle of incident x-ray radiation. In contrast, the ratio of the two peaks A and B at the M_5 edge [Fig. 3(a)] located at 1238.9 and 1240.1 eV shows a systematic increase with decreasing incident angle. This finding indicates an asymmetric occupation of the $4f$ states [16]. The observation of angular dependence of the spectra is surprising at first glance because the crystal fields acting on the localized $4f$ states were considered to be smaller than the experimental lifetime broadening. At low temperatures, however, the different crystal-field energies of tens of meV lead to an occupation asymmetry of the $4f$ states, which in turn causes a change of the relative contribution of unoccupied states to the multiplet structure of the spectra. The peak ratio of peaks A and B shows a monotonous decrease as a function of the incident angle within the error limits [Fig. 4(a)].

Angular variations of the XMCD spectra beyond changes of their magnitudes are not expected for reasonably small

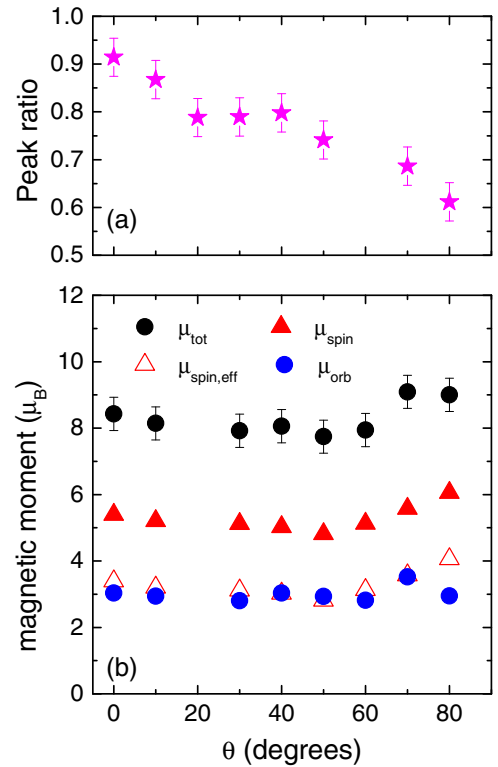


FIG. 4. (a) Ratio of the peak intensities of peaks A and B of the Tb absorption spectra as a function of the incident angle θ . (b) Tb magnetic moments $\mu_{spin,eff}$, μ_{spin} , μ_{orb} , and $\mu_{tot} = \mu_{spin} + \mu_{orb}$ as a function of θ .

crystal fields. In contrast, we observe distinct spectral changes in particular at the rising edge of the M_5 absorption edge (positive preedge peak). This might be attributed to the occurrence of a probing depth dependence and/or angular dependence of the saturation and self-absorption.

Figure 4(b) depicts the angular variation of spin and orbital moments. The experimentally determined values are almost independent on the angle of incidence.

The spin magnetic moment resulting from the sum-rule analysis [Fig. 4(b)], $\mu_{spin,eff} = 2(S_z + 3T_z)\mu_B$, contains the contribution from T_z . Hund's rules predict a value of $T_z = -0.333$ [40]. Numerical calculation reveals a ground-state value of $T_z = -0.243$ [35]. Because T_z has a negative value, the measured effective spin moment will be smaller than the pure spin magnetic moment. If the spin is fully aligned along the easy axis, the expectation value T_z according to Hund's rule will result in a reduction of the measured value effective spin moment by $2\mu_B$. For the case of grazing incidence ($\theta \rightarrow 90^\circ$), this correction leads to a maximum value of $\mu_{spin} = 6\mu_B$. The T_z term has negligible angular variation, which can be explained by the strong spin-orbit coupling, leading to a rotation of the T_z ellipsoid along with the rotation of the spin moment with respect to the molecular axis by the external field [44]. In this case, the effective spin moment always includes the spin-orbit-induced dipole term contribution independent of the molecular orientation. Our observation has an implication on powder measurements on randomly oriented molecules, where in that case the T_z term will not vanish due to averaging.

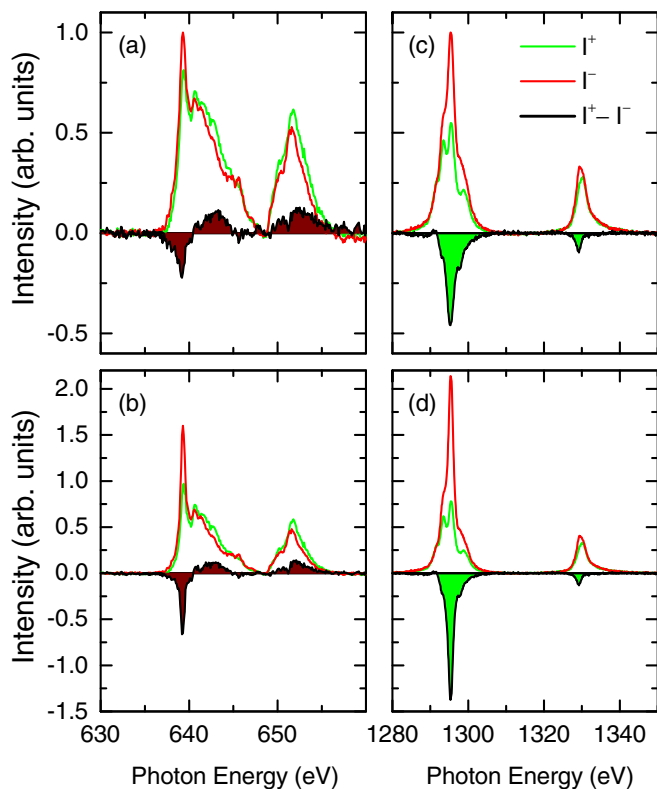


FIG. 5. (a) X-ray fluorescence intensity $I_{m,\parallel}$ as a function of photon energy at the Mn $L_{2,3}$ absorption edge in DyMn_4 . Spectra are measured for circularly polarized x-ray light parallel and antiparallel (I^+ , I^-) to the magnetic field. The XMCD signal calculated from the difference is depicted as a black line. (b) Corresponding Mn fluorescence signal Y_{\parallel} generated from the fluorescence spectra in panel (a) by Eq. (3). (c),(d) Similar data obtained at the Dy $M_{4,5}$ absorption edge in DyMn_4 . All spectra are measured at normal incidence.

In summary, the sum-rule analysis of the fluorescence yield spectra results in magnetic moments that are close to the expected ionic values, but one should take into account that the fluorescence process leads to spectra deviating from the absorption spectra and hence to magnetic moments deviating from the actual values. This will be discussed in more detail in the case of DyMn_4 .

B. DyMn_4

For the DyMn_4 single crystal, the self-absorption corrections for the XAS signals [Figs. 5(a) and 2(b)] have been performed in a similar way as for the TbMn_4 single crystal. In this case, the Mn spectrum appears as a combination of 90% Mn(II) and 10% Mn(III). Correspondingly, the Mn XMCD signal is slightly smaller than in the case of TbMn_4 due to the smaller contribution of Mn(II) ions.

After self-absorption correction, the Dy fluorescence signal [Figs. 5(c) and 5(d)] transforms into the typical Dy(III) $M_{4,5}$ edge XAS absorption spectrum. The Dy absorption spectrum shows a pronounced negative XMCD signal at the M_5 edge and a signal of negative sign at the M_4 edge. In this case, the sum-rule analysis reveals an effective spin magnetic moment of $2.5\mu_B$ and an orbital magnetic moment of $2.9\mu_B$.

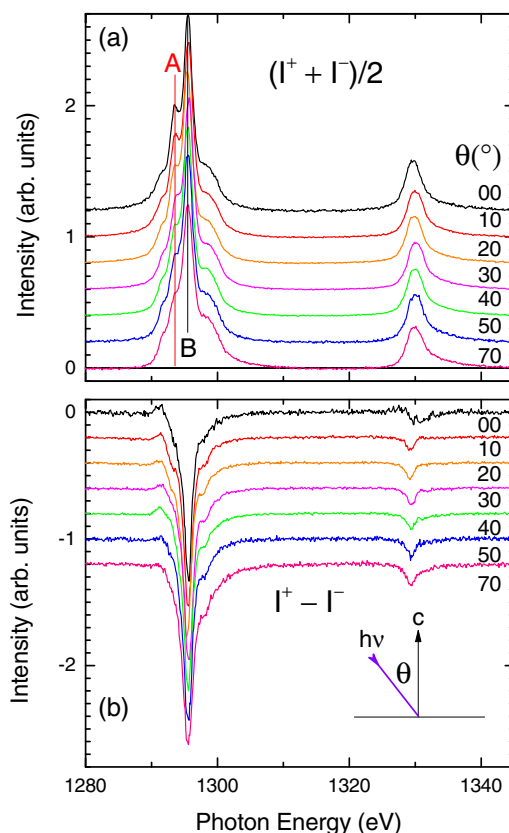


FIG. 6. (a) X-ray fluorescence spectra Y_{\parallel} at the Dy $M_{4,5}$ absorption edge in DyMn_4 ($I^+ + I^-$) measured at the indicated incident angles θ . (b) Corresponding XMCD spectra ($I^+ - I^-$).

The angular dependent Dy spectra are shown in Fig. 6. The spectral shape of Y_{\parallel} at the M_4 edge varies only little with the angle of incident x-ray radiation. As in the case of Tb, the ratio of the two peaks A and B at the M_5 edge [Fig. 6(a)] located at 1293.5 and 1295.6 eV shows a monotonous increase with decreasing incident angle [Fig. 8(a)]. This finding again indicates an asymmetric occupation of the 4f states. The explanation is similar to the case of Tb(III) discussed above.

The crystal field causes an anisotropic charge distribution of the 4f states deviating from spherical symmetric, which in turn results in an angular dependence of the fluorescence spectra. This effect was simulated by angular-dependent mixing of the circular left and right polarization with linear z-polarization in the calculated excitation spectra.

For the simulation of spectra, we take into account the part of the fluorescence signal that originates directly from the $3d - 4f$ x-ray emission spectrum and a second part from all other photon emission processes, being proportional to the x-ray absorption spectrum. This is justified by the good agreement of the angular dependence of simulated and experimental spectra.

Figure 7 shows the simulated $3d - 4f$ spectra assuming an equal contribution from direct $3d - 4f$ fluorescence photons and from photons stemming from other emission processes. The simulated data reproduce the variation of the spectral feature A at the M_5 edge with angle θ , confirming the

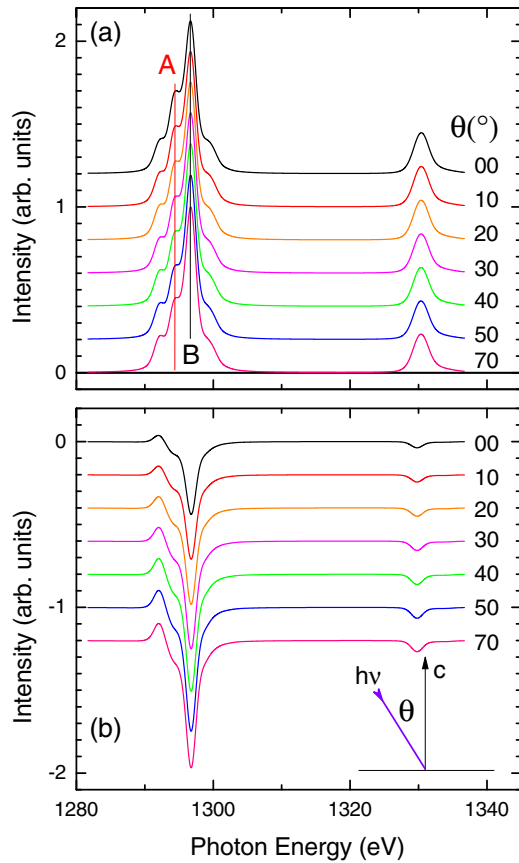


FIG. 7. (a) Simulated x-ray fluorescence intensity at the Dy $M_{4,5}$ absorption edge as a function of incident angle θ assuming 50% contribution from normal x-ray absorption and 50% contribution from $3d4f$ fluorescence yield. (b) Corresponding XMCD spectra.

crystal-field-induced asymmetric probability density of the $4f$ states. The XMCD maxima and minima increase in size with increasing angle θ without changing their spectral features, similar to the experimental behavior.

Figure 8(b) depicts the angular variation of spin and orbital moments as derived from the experimental spectra Y_{\parallel} . In the case of Dy(III), the ionic value for the orbital magnetic moment is $5\mu_B$. The experimentally determined value increases from $3\mu_B$ for perpendicular incidence to $5\mu_B$ for $\theta = 80^\circ$.

The effective spin magnetic moment [Fig. 8(b)], $\mu_{\text{spin,eff}} = 2(S_z + 3T_z)\mu_B$, contains also in the case of Dy the contribution from T_z . The maximum value of T_z can be estimated from the difference between the effective spin moment and the expected pure spin moment of $5\mu_B$ measured close to grazing incidence, i.e., with the field applied along the easy axis. This difference amounts to $1.2\mu_B$, indicating $T_z = -0.2$. This value seems reasonable because it lies in between Hund's rule value (-0.332) [40] and the numerical calculation ($T_z = -0.128$) [35].

The total Dy moment resulting from the sum of the orbital and the spin moment increases from perpendicular incidence to grazing incidence. The maximum value obtained for grazing incidence is $11\mu_B$, which is larger than the ionic value of $10\mu_B$.

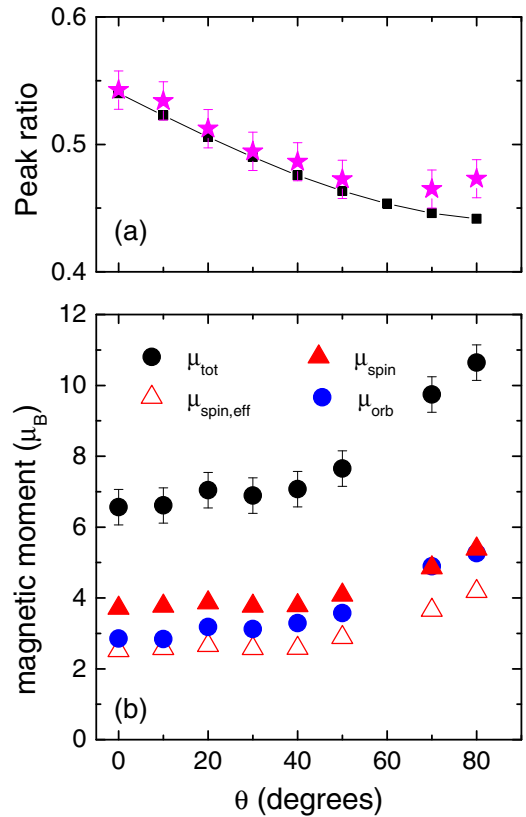


FIG. 8. (a) Ratio of the peak intensities of peaks A and B of the Dy absorption spectra as a function of the incident angle θ in comparison with simulated values (black dots). (b) Dy magnetic moments $\mu_{\text{spin,eff}}$, μ_{spin} , μ_{orb} , and $\mu_{\text{tot}} = \mu_{\text{spin}} + \mu_{\text{orb}}$ as a function of θ .

To discuss the influence of the fact that we measure fluorescence spectra in contrast to electron yield spectra, we discuss magnetic moments obtained from a sum-rule analysis of the simulated spectra. Figure 9(a) shows the corresponding results obtained from the simulated spectra shown in Fig. 7. Spin and orbital moments increase with increasing angle θ . The absolute values obtained from the simulated fluorescence spectra deviate from the magnetic moments resulting from simulated electron yield XAS/XMCD data, which are then close to the expected ionic values. This deviation of moments determined either from electron yield or from fluorescence yield is due to the final state dependence of the fluorescence decay.

For a quantitative determination of magnetic moments from the measured fluorescence data, we derive angular-dependent correction factors for spin and orbital moments given by the ratio of the ionic values and the sum-rule-derived moments from the simulated fluorescence data. The spin and orbital moments derived from the sum-rule analysis of the experimental spectra (see Fig. 8) are then multiplied by this correction factor. This correction also takes care of the expectation value of the dipole operator T_z contributing to μ_{spin} . The results shown in Fig. 9(b) reveal values for spin and orbital moments. The experimental magnetic moments are smaller than the ionic values. This reduction originates from the presence of the crystal field in combination with the

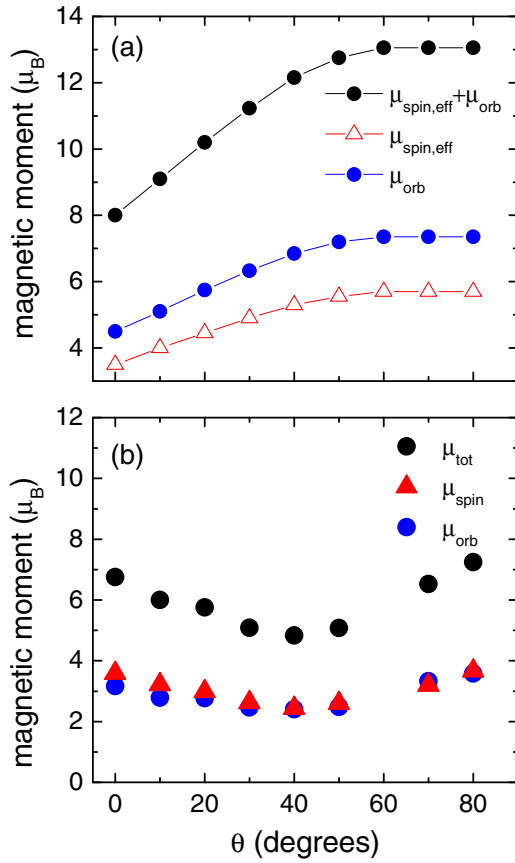


FIG. 9. (a) Dy magnetic moments $\mu_{\text{spin,eff}}$, μ_{orb} , and the sum of both values as a function of θ derived from a sum-rule analysis of the simulated spectra. (b) Corrected spin, orbital, and total magnetic moments of Dy.

finite temperature and field of the experiment, as discussed below. The reduction is in fair agreement with experimental results obtained on polycrystalline material of the same molecules [33].

Even after the correction, the sum of spin and orbital magnetic moments [Fig. 9(b)] shows a significant variation with angle θ . We observe a minimum at $\theta = 40^\circ$, where the magnetic moment is reduced by 30% with respect to the larger values observed for perpendicular and grazing incidence. We attribute this angular dependence to the magnetic anisotropy that has not been considered in Eq. (1). The minimum close to 45° indicates a fourth-order anisotropy term, with the preferred direction of magnetization along the fourfold symmetry axis or perpendicular to it. The smallest magnetic moment lies between these two directions indicating a magnetic hard axis.

Electrostatic interactions qualitatively explain the occurrence of the fourth-order magnetic anisotropy. Figure 10(a) depicts the interaction of the crystal field with the charge distribution of the Dy(III) and Tb(III) 4f states. The pyramidal ligand orientation is generalized by an octahedral field with a small tetragonal distortion. The Dy 4f charge distribution resembles a barrel. If the symmetry axis is oriented at $\theta = 45^\circ$, the barrel edges will approach the surrounding ligand charges and thus increase the electrostatic energy and contribute to the magnetic anisotropy. Accordingly, the energy is lowered for $\theta = 0^\circ$ and 90° .

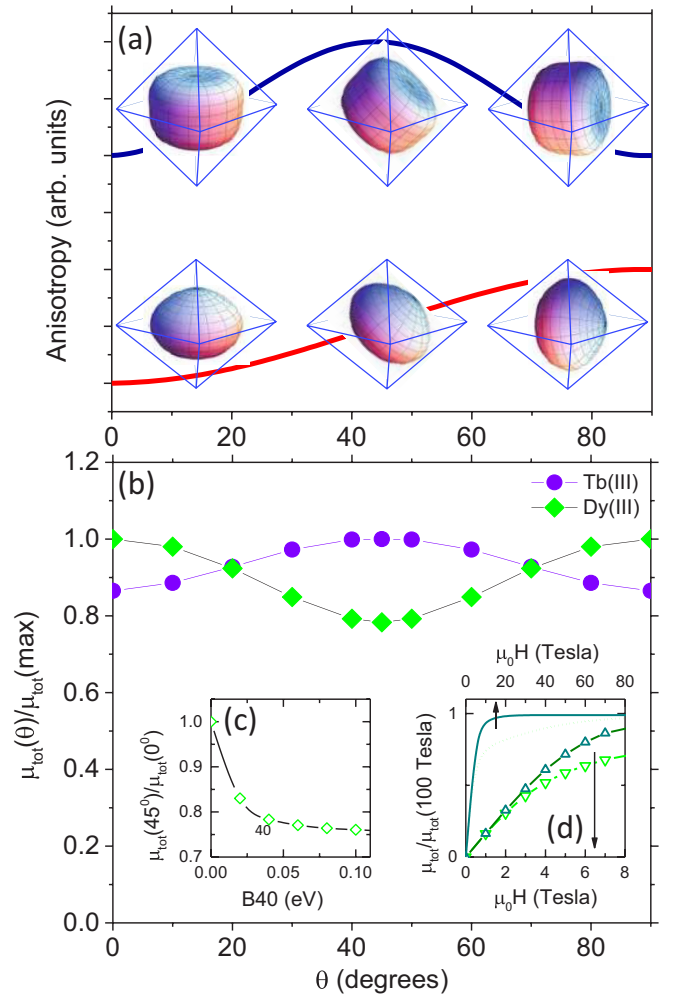


FIG. 10. (a) Sketch of second-order (red line, easy axis $\theta = 0^\circ$) and fourth-order (blue line, easy axes at $\theta = 0^\circ$ and 90°) magnetic anisotropies contributing to the free energy. The oblate charge distribution of Tb(III) 4f states (lower row) causes an increase of the electrostatic energy in a tetragonally distorted octahedral crystal field for $\theta = 90^\circ$. The barrel-like Dy(III) 4f charge distribution (upper row) causes a maximum electrostatic energy for $\theta = 45^\circ$ even for a pure octahedral crystal field. The 4f charge distributions are modified from Ref. [49]. (b) Magnetic moments derived from multiplet calculations for Tb(III) (bullets) and Dy(III) (diamonds) in an octahedral crystal field ($B_{40} = 0.04 \text{ eV}$, $B_{60} = 0$) as a function of θ for $T = 14 \text{ K}$ and $\mu_0 H = 7 \text{ T}$. (c) Calculated reduction of Dy(III) magnetic moment along the magnetic hard axis as a function of crystal-field parameter B_{40} for $T = 14 \text{ K}$ and $\mu_0 H = 7 \text{ T}$. (d) Calculated magnetization curve for $B_{40} = 0.04 \text{ eV}$, $B_{60} = 0$, and $T = 14 \text{ K}$ for $\theta = 0^\circ$ (up-triangles, full lines) and $\theta = 45^\circ$ (down-triangles, dotted lines). Magnetization curves are shown with respect to an extended (top axis, lines) and expanded (bottom axis, symbols) field range. The expanded field range reveals the saturation fields.

For Tb(III), we assume that the fluorescence spectra will also result in an apparently increasing moment with increasing θ , similar to the behavior shown in Fig. 9(a) for Dy(III). The correction of the Tb moments shown in Fig. 4(b) will then result in larger Tb moments and hence a magnetic easy axis at $\theta = 0^\circ$ for the case of TbMn₄. In the case of Tb(III), the oblate

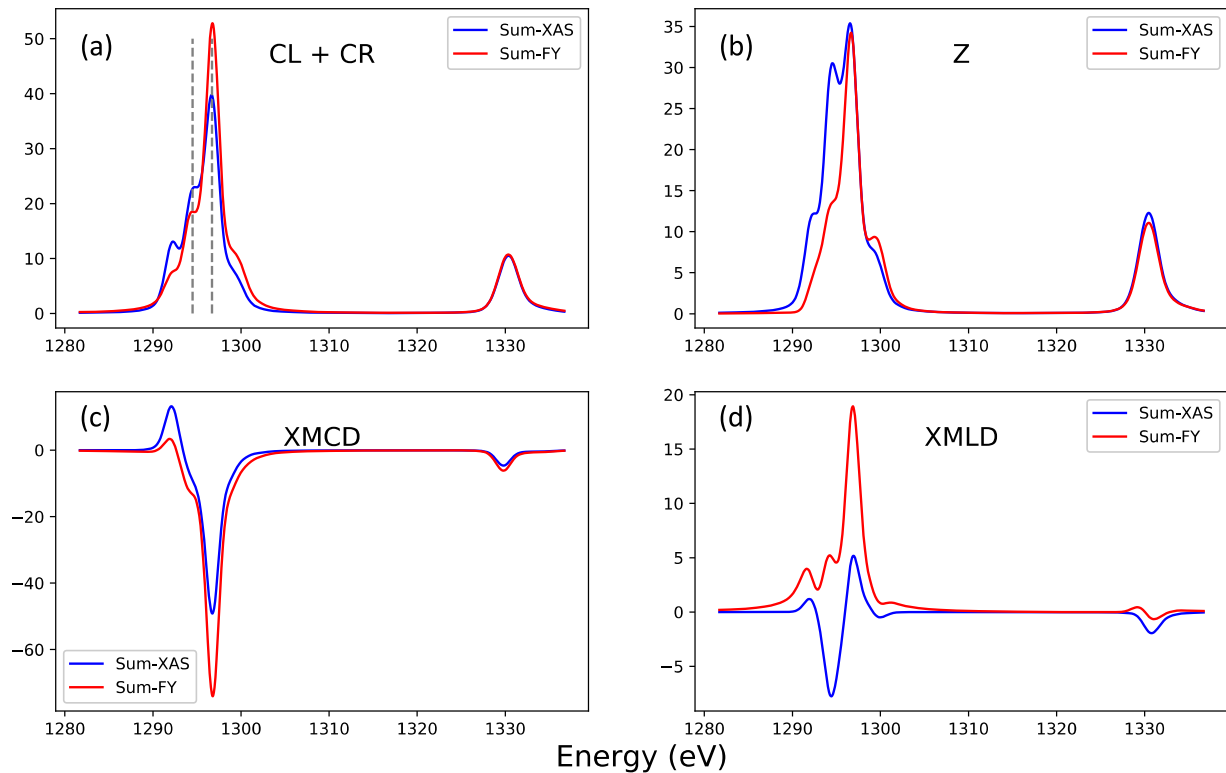


FIG. 11. Comparison of simulated x-ray absorption (blue) and fluorescence (red) spectra at 7 K. (a) Sum of intensities obtained for circular left (CL) and right (CR) polarization. (b) Intensity for linear polarized light along the z -axis (Z-component). (c) XMCD signals calculated from the difference of CL and CR. (d) X-ray linear dichroism (XMLD) calculated from the difference of the CL/CR sum signal and the Z-component.

ellipsoidal charge distribution leads to an energy minimum for perpendicular symmetry axis orientation. The electrostatic energy and hence the magnetic anisotropy increase with increasing θ . This suggests a uniaxial magnetic anisotropy with an easy axis along $\theta = 0^\circ$ in agreement with the experimental finding.

To substantiate this pictorial view, we performed multiplet calculations for spectral data including an octahedral crystal field introducing the crystal-field parameters B_{40} and B_{60} . Crystal-field-related changes of XMCD spectra appear as a common factor, resulting in a constant spin to orbital moment ratio and reflecting variations of magnetic moments. Using crystal-field parameters $B_{40} = 0.04$ eV and $B_{60} = 0$, Tb(III) and Dy(III) ions show an opposite sign of the fourth-order magnetic anisotropy constant [see Fig. 10(b)]: While the angular dependence of the Dy(III) moment reveals a minimum at $\theta = 45^\circ$, indicating a hard axis direction, the Tb(III) moment shows a maximum at this angle. An opposite sign of the fourth-order anisotropy constant can be expected from the different $4f$ charge distribution of Dy(III) and Tb(III) ions as qualitatively depicted in Fig. 10(a). In the case of Dy(III), the magnetic moment reduction along the hard axis at $\theta = 45^\circ$ increases nonlinearly with increasing crystal-field parameter B_{40} [see Fig. 10(c)]. The calculated magnetization curves for easy- and hard-axis orientation reveal the impact of the crystal field on the magnetization curve. At $T = 14$ K and in a field of 7 T, the moment is reduced between 60% and 80% with respect to the ionic value, which is in fair agreement with the experimental observation.

We note that it is not possible to determine crystal-field parameters from the geometry of the molecule because of the nonlocal charge distribution of the valence orbitals. Nevertheless, the agreement of multiplet calculations including crystal-field parameters with the experimental results substantiates the suggested ionic-type origin of the fourth-order magnetic anisotropy.

V. CONCLUSION AND SUMMARY

To conclude, the detection of the x-ray fluorescence signal instead of the total electron yield in x-ray absorption spectroscopy is a valuable tool to investigate magnetic properties of single-crystal SMMs. The pronounced self-absorption of x-ray fluorescence can be compensated by a correction model. The self-absorption effect is particularly small in molecular single crystals where the concentration of magnetic cores is small. Moreover, the fluorescence signal is measurable on typically insulating molecular single crystals, in contrast to the total electron yield.

The fluorescence yield x-ray absorption spectrum deviates from the spectrum measured by electron yield. While the electron yield spectrum reflects the standard x-ray absorption spectrum, the fluorescence yield spectrum is dominated by the integrated $3d4f$ resonant inelastic x-ray scattering spectrum. Using crystal-field multiplet calculations, fluorescence yield and absorption spectra can be simulated. The actual measured fluorescence yield spectrum is a mixture of the calculated $3d4f$ fluorescence yield spectrum and the

normal x-ray absorption spectrum. A sum-rule analysis of the simulated spectra allows for a correction of the sum-rule-derived magnetic moments obtained from the experimental data.

In summary, x-ray fluorescence spectroscopy reveals angular-dependent element-specific magnetic moments in $3d-4f$ single molecular magnets at low temperature (14 K) and large field (7 T). The Mn x-ray absorption spectra indicate an ionic Mn(II) instead of the expected Mn(III) state, which we attribute to an x-ray-induced reduction mechanism. The molecular magnetic moment is dominated by the rare-earth moment revealing a considerable large contribution of orbital moment. The sum-rule analysis of the rare-earth moments results in a good agreement with the expected ionic values considering the finite temperature. From the angular-dependent spectra on the oriented molecules in single crystals, we conclude on magnetic anisotropies. The magnetic anisotropy is a fourth-order anisotropy revealing easy directions parallel and perpendicular to the plane formed by the 4 Mn ions. A simple model considering a Coulomb interaction of the $4f$ anisotropic charge distribution with the ligand field qualitatively explains the occurrence of the fourth-order anisotropy. Multiplet calculations suggest that the fourth-order anisotropy of Dy(III) originates from a crystal-field parameter $B_{40} = 0.04$ eV.

ACKNOWLEDGMENTS

Funding by the Deutsche Forschungsgemeinschaft (DFG, German Research Foundation)–TRR 173–268565370 (Project No. A09) is gratefully acknowledged. The authors acknowledge financial support for the VEKMAG project and for the PM2-VEKMAG beamline by the German Federal Ministry for Education and Research (BMBF 05K10PC2, 05K10WR1, 05K10KE1) and by HZB. Steffen Rudorff is acknowledged for technical support.

APPENDIX: COMPARISON OF X-RAY ABSORPTION AND FLUORESCENCE SPECTRA

Figure 11 shows a comparison between simulated x-ray absorption spectra and simulated x-ray fluorescence spectra. Note the pronounced spectral difference in the Z-component [Fig. 11(b)] leading to the angular variation of the fluorescence signal. In contrast, the Z-component of the x-ray absorption spectrum shows smaller differences from the circular left and right (CL,CR) components. The difference in the XMCD signals is only given by the magnitude of the signal [Fig. 11(c)]. The simulation also predicts a significant linear dichroism (XMLD) beyond the spectral magnitude [Fig. 11(d)].

-
- [1] C. Y. Chow, E. R. Trivedi, V. Pecoraro, and C. M. Zaleski, *Comments Inorg. Chem.* **35**, 214 (2015).
- [2] C. Y. Chow, S. V. Eliseeva, E. R. Trivedi, T. N. Nguyen, J. W. Kampf, S. Petoud, and V. L. Pecoraro, *J. Am. Chem. Soc.* **138**, 5100 (2016).
- [3] F. Evangelisti, R. More, F. Hodel, S. Lubner, and G. R. Patzke, *J. Am. Chem. Soc.* **137**, 11076 (2015).
- [4] L. Rosado Piquer and E. C. Sanudo, *Dalton Trans.* **44**, 8771 (2015).
- [5] D. N. Woodruff, R. E. P. Winpenny, and R. A. Layfield, *Chem. Rev.* **113**, 5110 (2013).
- [6] G. Christou, D. Gatteschi, D. N. Hendrickson, and R. Sessoli, *MRS Bull.* **25**, 66 (2000).
- [7] C. F. Hermanns, M. Bernien, A. Krüger, W. Walter, Y.-M. Chang, E. Weschke, and W. Kuch, *Phys. Rev. B* **88**, 104420 (2013).
- [8] Y.-N. Guo, G.-F. Xu, Y. Guo, and J. Tang, *Dalton Trans.* **40**, 9953 (2011).
- [9] J. R. Friedman, M. P. Sarachik, J. Tejada, and R. Ziolo, *Phys. Rev. Lett.* **76**, 3830 (1996).
- [10] L. Thomas, F. Lioni, R. Ballou, D. Gatteschi, R. Sessoli, and B. Barbara, *Nature (London)* **383**, 145 (1996).
- [11] L. Bogani and W. Wernsdorfer, *Nat. Mater.* **7**, 179 (2008).
- [12] M. Urdampilleta, S. Klyatskaya, J.-P. Cleuziou, M. Ruben, and W. Wernsdorfer, *Nat. Mater.* **10**, 502 (2011).
- [13] E. Coronado, *Nat. Rev. Mater.* **5**, 87 (2020).
- [14] Y. Lan, S. Klyatskaya, M. Ruben, O. Fuhr, W. Wernsdorfer, A. Candini, V. Corradini, A. Lodi Rizzini, U. del Pennino, F. Troiani, L. Joly, D. Klar, H. Wende, and M. Affronte, *J. Mater. Chem. C* **3**, 9794 (2015).
- [15] J.-L. Liu, Y.-C. Chen, and M.-L. Tong, *Chem. Soc. Rev.* **47**, 2431 (2018).
- [16] P. Hansmann, A. Severing, Z. Hu, M. W. Haverkort, C. F. Chang, S. Klein, A. Tanaka, H. H. Hsieh, H. J. Lin, C. T. Chen, B. Fak, P. Lejay, and L. H. Tjeng, *Phys. Rev. Lett.* **100**, 066405 (2008).
- [17] M. S. Lah, M. L. Kirk, W. Hatfield, and V. L. Pecoraro, *J. Chem. Soc. Chem. Commun.* **21**, 1606 (1989).
- [18] M. S. Lah and V. L. Pecoraro, *J. Am. Chem. Soc.* **111**, 7258 (1989).
- [19] J. C. Dutton, K. S. Murray, and E. R. Tiekink, *Inorg. Chim. Acta* **166**, 5 (1989).
- [20] G. Mezei, C. M. Zaleski, and V. L. Pecoraro, *Chem. Rev.* **107**, 4933 (2007).
- [21] M. Tegoni, M. Furlotti, M. Tropiano, C. S. Lim, and V. L. Pecoraro, *Inorg. Chem.* **49**, 5190 (2010).
- [22] P. Happ and E. Rentschler, *Dalton Trans.* **43**, 15308 (2014).
- [23] P. Happ, C. Plenck, and E. Rentschler, *Coord. Chem. Rev.* **289-290**, 238 (2015).
- [24] C. Plenck, J. Krause, M. Beck, and E. Rentschler, *Chem. Commun.* **51**, 6524 (2015).
- [25] P. Happ, A. Sapozhnik, J. Klanke, P. Czaja, A. Chernenkaya, K. Medjanik, S. Schuppler, P. Nagel, M. Merz, E. Rentschler, and H. J. Elmers, *Phys. Rev. B* **93**, 174404 (2016).
- [26] A. A. Athanasopoulou, C. Gamer, L. Völker, and E. Rentschler, in *Novel Magnetic Nanostructures* (Elsevier, 2018), pp.51–96.
- [27] A. Alhassanat, I. C. Gamer, A. Rauguth, A. A. Athanasopoulou, J. Sutter, C. Luo, H. Ryll, F. Radu, A. A. Sapozhnik, T. Mashoff, E. Rentschler, and H. J. Elmers, *Phys. Rev. B* **98**, 064428 (2018).

- [28] A. Alhassanat, L. Voelker, C. Gamer, A. Rauguth, A. Kredel, C. Luo, F. Radu, A. A. Sapozhnik, T. Mashoff, E. Rentschler, and H. J. Elmers, *Phys. Rev. B* **99**, 104404 (2019).
- [29] A. A. Athanasopoulou, J. J. Baldovi, L. M. Carrella, and E. Rentschler, *Dalton Trans.* **48**, 15381 (2019).
- [30] C. Luo, H. Ryll, and F. Back, C. H. Radu, *Sci. Rep.* **9**, 18169 (2019).
- [31] F. de Groot, M. Arrio, P. Saintavit, C. Cartier, and C. Chen, *Solid State Commun.* **92**, 991 (1994).
- [32] B. Liu, C. Piamonteze, M. U. Delgado-Jaime, R.-P. Wang, J. Heidler, J. Dreiser, R. Chopdekar, F. Nolting, and F. M. F. de Groot, *Phys. Rev. B* **96**, 054446 (2017).
- [33] A. A. Athanasopoulou, L. M. Carrella, and E. Rentschler, *Inorganics* **6**, 66 (2018).
- [34] T. Noll and F. Radu, *Proc. MEDSI2016* (JACoW Publishing, Geneva, Switzerland, 2017), pp. 370–373.
- [35] Y. Teramura, A. Tanaka, and T. Jo, *J. Phys. Soc. Jpn.* **65**, 3056 (1996).
- [36] T. Jo, *J. Electron Spectrosc. Relat. Phenom.* **86**, 73 (1997).
- [37] N. Grumbach, A. Barla, L. Joly, B. Donnio, G. Rogez, E. Terazzi, J. P. Kappler, and J. L. Gallani, *Eur. Phys. J. B* **73**, 103 (2010).
- [38] M. Mannini, F. Pineider, P. Saintavit, L. Joly, A. Fraile-Rodriguez, M.-A. Arrio, C. C. d. Moulin, W. Wernsdorfer, A. Cornia, D. Gatteschi, and R. Sessoli, *Adv. Mater.* **21**, 167 (2009).
- [39] M. Mannini, P. Saintavit, R. Sessoli, C. C. d. Moulin, F. Pineider, M.-A. Arrio, A. Cornia, and D. Gatteschi, *Chem. Eur. J.* **14**, 7530 (2008).
- [40] P. Carra, B. T. Thole, M. Altarelli, and X. Wang, *Phys. Rev. Lett.* **70**, 694 (1993).
- [41] B. T. Thole, P. Carra, F. Sette, and G. van der Laan, *Phys. Rev. Lett.* **68**, 1943 (1992).
- [42] E. Stavitski and F. M. F. de Groot, *Micron* **41**, 687 (2010).
- [43] S. Tripathi, Ph.D. thesis, University Stuttgart (2018)
- [44] N. Y. Schmidt, S. Laureti, F. Radu, H. Ryll, C. Luo, F. d'Acapito, S. Tripathi, E. Goering, D. Weller, and M. Albrecht, *Phys. Rev. B* **100**, 064428 (2019).
- [45] J. B. Goedkoop, J. C. Fuggle, B. T. Thole, G. van der Laan, and G. A. Sawatzky, *J. Appl. Phys.* **64**, 5595 (1988).
- [46] J. B. Goedkoop, B. T. Thole, G. van der Laan, G. A. Sawatzky, F. M. F. de Groot, and J. C. Fuggle, *Phys. Rev. B* **37**, 2086 (1988).
- [47] M. W. Haverkort, M. Zwierzycki, and O. K. Andersen, *Phys. Rev. B* **85**, 165113 (2012).
- [48] R. Nakajima, J. Stohr, and Y. Idzerda, *Phys. Rev. B* **59**, 6421 (1999).
- [49] S. Jiang, W. Wang, and S. Gao, *Advances in Lanthanide Single-Ion Magnets, in Molecular Nanomagnets and Related Phenomena*, edited by S. Gao (Springer, Berlin, 2015).